Quantification of Acoustic Radiation Forces on Solid Objects in Fluid

Mohamed A. Ghanem,[1,*] Adam D. Maxwell,[2] Oleg A. Sapozhnikov,[1,3] Vera A. Khokhlova,[1,3] and Michael R. Bailey[1]

[1] *Applied Physics Laboratory, Center for Industrial and Medical Ultrasound, University of Washington, Seattle, Washington 98105, USA*

[2] *Department of Urology, School of Medicine, University of Washington, Seattle, Washington 98195, USA*

[3] *Physics Faculty, Moscow State University, 119991, Moscow, Russia*

(Received 10 June 2019; revised manuscript received 9 September 2019; published 31 October 2019)

Theoretical models allow design of acoustic traps to manipulate objects with radiation force. A model of the acoustic radiation force by an arbitrary beam on a solid object is validated against measurement. The lateral force in water of different acoustic beams is measured and calculated for spheres of different diameters (2–6 wavelengths λ in water) and compositions. This is the first effort to validate a general model, to quantify the lateral force on a range of objects, and to electronically steer large or dense objects with a single-sided transducer. Vortex beams and two other beam shapes having a ring-shaped pressure field in the focal plane are synthesized in water by a 1.5-MHz, 256-element focused array. Spherical targets (glass, brass, ceramic, 2–6 mm dia.) are placed on an acoustically transparent plastic plate that is normal to the acoustic beam axis and rigidly attached to the array. Each sphere is trapped in the beam as the array with the attached plate is rotated until the sphere falls from the acoustic trap because of gravity. Calculated and measured maximum obtained angles agree on average to within 22%. The maximum lateral force occurs when the target diameter equals the beam width; however, objects up to 40% larger than the beam width are trapped. The lateral force is comparable to the gravitation force on spheres up to 90 mg (0.0009 N) at beam powers on the order of 10 W. As a step toward manipulating objects, the beams are used to trap and electronically steer the spheres along a two-dimensional path.

DOI: 10.1103/PhysRevApplied.12.044076

I. INTRODUCTION

The 2018 Nobel Prize in Physics was awarded to Ashkin for his seminal work on optical tweezers [1,2] to trap and to move an object with a beam of light. To create this effect, a laser was focused on a transparent object that refracted the beam such that the net radiation force on the object pushed or pulled the object to a specific point in the beam. While early work used refraction as a primary means to produce trapping, radiation force can also be produced by scattering or absorption of the wave by the object. Optical tweezers have enabled manipulation of living cells [3,4] to measure cell properties and unfold DNA [5], as well as to trap atoms [6,7] in order to, for example, improve the accuracy of atomic clocks [8].

Similar to electromagnetic waves, acoustic waves can apply radiation forces [9–11] to trap and to manipulate objects. Moreover, as radiation force is proportional to the power of the wavefield incident on an object divided by the wave speed [12], radiation forces in acoustics are orders of magnitude larger than in optics. Acoustic traps are versatile; they can be employed in different media, such as air [13–15] and water [16,17] for a variety of applications, such as cell sorting [18,19] and targeted drug delivery [20]. Therefore, there is an increasing interest in understanding and expanding the conditions for which acoustic traps can be employed.

Here, we report experimental validation of a general theoretical model for designing acoustic tweezers, a measurement of the lateral trapping forces from acoustic beams on a range of objects, and a demonstration of electronically steering an object larger than the wavelength by such forces. Early theoretical work by Gor'kov [21] calculated the acoustic radiation forces on particles much smaller than the wavelength in a standing or traveling wavefield by calculating the scattered field. For small particles, Gor'kov recognized that the monopole and dipole terms that correspond to the compressibility and density of the object could accurately describe the scattered field, which is not the case for larger objects. Small particles have been experimentally trapped and manipulated in the pressure nodes of a standing wave generated by a transducer and a reflector [22–24] or multiple transducers facing each other [14].

Single-sided trapping has also been achieved. In single-sided trapping, multielement arrays generate and steer acoustic beams by controlling the phasing between the

*mghanem@uw.edu

array elements. Many theoretical studies have focused on using vortex beams [25–27], which are replicated experimentally by exciting the array elements with linearly increasing circumferential delays in order to generate an annular pressure field in the focal plane that can surround and trap objects. Calculations show an idealized, nondiffracting, vortex beam is theoretically capable of pushing, pulling [28,29], and trapping rigid [30] and elastic [31,32] spheres. Experimentally, vortex beams have been used to trap and pull small polystyrene spheres (190 μm, 0.3λ) in water while recording their motion to determine the axial radiation forces [17]. Beyond vortex beams, twin and bottle beams have been used experimentally to trap and to move an expanded polystyrene sphere (1 mm, 0.12λ) in air [15]. Simultaneous traps have also been created by a single source to steer multiple particles independently of each other [33]. However, trapping and manipulation of particles in three-dimensional (3D) space by a single-sided source have been limited to particles smaller than a wavelength.

Development and experimental validation of trapping objects equal to or larger than the wavelength have been limited to specific conditions. Successful levitation of a large expanded polystyrene sphere (50 mm, 3.6λ) in air was achieved by creating a standing wave between the sphere and a three-element source [34]. Similar to Ashkin's work [1,2], a ray acoustics model was developed [35,36] to predict the trapping forces of a focused beam on spheres with a lower sound speed than the surrounding fluid, which is optically equivalent to an object with greater index of refraction than the medium. The model was experimentally tested in the pulling of lipid droplets radially along a transverse focal plate toward the acoustic axis (126 μm, 2.5λ) [37] and polystyrene microspheres (10 μm, 1.3λ) [38] in water. Most recently, successful trapping of a large expanded polystyrene sphere (16 mm, 1.85λ) in air using a vortex beam was demonstrated [39]. Although these studies have shown the feasibility of achieving control of large spheres in specific cases, a more general development and experimental verification of acoustic tweezers to manipulate large particles has not been performed.

Most theoretical solutions have been obtained for radiation forces on spheres in specific beams. The models come down to calculating the scattered field and then integrating over this field around the sphere to obtain the radiation forces. The scattered field and corresponding radiation forces have been calculated for idealized fields, such as plane waves [10,40,41] or nondiffracting beams [42–46] including unfocused vortex beams [28–32]. Sapozhnikov and Bailey published the first modeling algorithm [47] (SB model) that resolved the acoustic radiation forces produced by an arbitrary acoustic field on a spherical elastic object of any size at any location in the field using an angular spectrum approach. Baresch *et al.* [48] and Jerome *et al.* [49] have developed similarly capable models. Baresch *et al.* derived similar solutions using spherical coordinates and reported agreement with the SB model in quantifying the radiation forces on spheres smaller than the wavelength [17]. Jerome *et al.* used Lagrangian coordinates [49], while the SB model uses Eulerian coordinates, and also reported agreement with SB model.

This paper reports on work to synthesize various acoustic beams in water and to use the SB model and measurement to quantify the lateral acoustic radiation forces on solid spherical targets of different composition and diameter. Furthermore, stable trapping and steering of these large targets is demonstrated toward a more general development of acoustic tweezers.

II. METHODS

A brief summary of the theoretical basis for the SB model is presented. The experimental setup for the measurement and validation of the lateral acoustic radiation forces is described. Finally, details of the stable trapping and dynamic steering experiment are explained.

A. Theoretical model

In the SB model, the angular spectrum formulation is used to decompose the incident acoustic beam to a sum of plane waves. The net scattered field is found from the summation of the scattering of each plane wave from a spherical object using the classical expression for the spherical harmonic scattering [50,51]. The incident and scattered fields are summed and integrated over a spherical surface that surrounds the object in order to calculate the change in the wave momentum and resulting radiation force.

Wave attenuation and viscous effects are not included here. While attenuation of the acoustic wave can be accounted for in the SB model by using a complex wavevector k, attenuation loss for a plane wave passing a plate of the thickness and composition of the spheres in this study is less than 7% [52]. Viscous losses around targets are also negligible since the viscous boundary layer δ is smaller than λ by approximately four orders of magnitude ($\delta = 0.46$ μm) [11]. While only spheres are used in this study, radiation force may be calculated for nonspherical objects following the same formalism with, for example, a finite element approach [53,54].

Figure 1 shows example calculations, where the axial F_{Az} and lateral F_{Ax} components of the acoustic radiation force are calculated for two spheres of one composition but different radii at different radial positions.

B. Lateral force measurement

The transducer used in our experiments is a piezocomposite, 1.5-MHz, 256-element, focused array (Imasonic, Voray sur l'Ognon, France) [55] with the elements

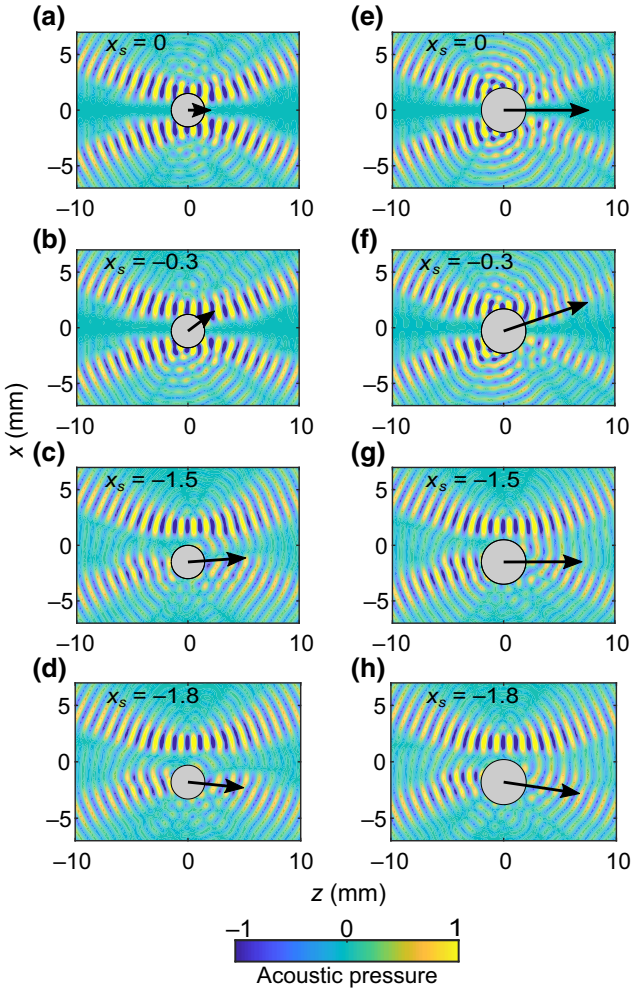

FIG. 1. Simulation illustrating the acoustic radiation force from the same vortex beam on 3-mm (a)–(d) and 4-mm (e)–(h) diameter solid glass spheres located near the acoustic beam axis. The acoustic wave propagates from left to right in the z direction, and with the color pattern displays the distribution of the instantaneous pressure. The location of the center of the sphere is indicated by x_s in mm. The arrow indicates the direction and magnitude of the acoustic radiation force, which comprises the x and y components. Depending on the sphere's radial location, the resulting acoustic force either restores the sphere toward the center of the beam as in (b),(f) or pushes the sphere out of the beam as in (d),(h).

arranged in 16 spirals of 16 elements each. The diameter of each element is 7 mm with interelement gaps of 0.5 mm. The transducer has a 12-cm radius of curvature, 15-cm aperture, and 4-cm diameter of the central opening. The face of the transducer is acoustically matched to water through a quarter-wavelength matching layer. The array elements are electrically matched with inductors at 1.5 MHz and driven using a Verasonics Data Acquisition System (V1, Verasonics, LTD., Kirkland, WA) and a research ultrasound engine with a 1200-W external power source (QPX600DP, Aim-TTI, Cambridgeshire, UK). Acoustic holography and a radiation force balance have been used previously to equalize the vibrational output for each element and to characterize the acoustic power and focal pressure of the array [56]. For reference, the maximum acoustic power used in any of our experiments is 12.8 W, the maximum peak pressure is 1.2 MPa, and the maximum spatial peak time-averaged intensity is 62 W/cm^2.

Three different acoustic beams are generated by varying the phase of each element of the array. The beams are designed to create a null pressure region on the array axis in the focal plane surrounded by a ring or rings of pressure. The beams, named here "vortex," "π radial," and "2π-radial" beams, are synthesized as shown in Fig. 2. For the vortex beams, the phase increases linearly around the array's azimuth angle to a maximum delay of $2\pi M$, where M is an integer known as the topological charge. The magnitude of M controls the ring width, and the sign of M controls the wavefront helicity. The π and 2π-radial beams are synthesized using an iterative angular spectrum approach (IASA) [57,58], where we input the desired ring-shaped pattern in the focal plane, and the IASA algorithm iteratively converges to a phase profile at the source that produced such a pattern, while for this work, maintaining uniform amplitude across the source surface. After a solution is found, the focal pressure distribution is back-propagated [59] to determine the phase at the center of each element [56]. Unlike the vortex beams, where the phase changes with the array's azimuth angle, for the π and 2π-radial beams, the phase changes strictly in the radial direction. The π radial beam is shown in the second row of Fig. 2 and has a single π phase shift along the radial direction. The 2π-radial beam is shown in the third row of Fig. 2 and has a two π phase shifts along the radial direction.

The strength of the lateral acoustic radiation force of different beams is measured by placing spherical targets of different sizes and compositions in the center of the beam as shown in Fig. 3. The spherical targets are placed on an acoustically transparent, flat, 6.4-mm, low-density polyethylene (LDPE) plate attached to the array by a frame. The frame-array combination is attached to a rotational stage and rotated slowly about the y axis at a maximum speed of 1°/s or 4 mm/s. As the angle of rotation and slope of the platform increase, the sphere rolls outward from the beam axis toward a point of a higher lateral acoustic radiation force. The sphere is held off axis by the total lateral force, which includes the lateral acoustic force as well as the added friction from a nonzero axial acoustic force F_{Az} into the plate, Fig. 3. Further rotation increases the gravitational component along the plate until it overcame the lateral forces and the sphere falls from the acoustic trap. The angle of maximum total lateral force $\theta_{\max}$ at which the sphere falls is recorded from measurements to each side and compared to calculations. The

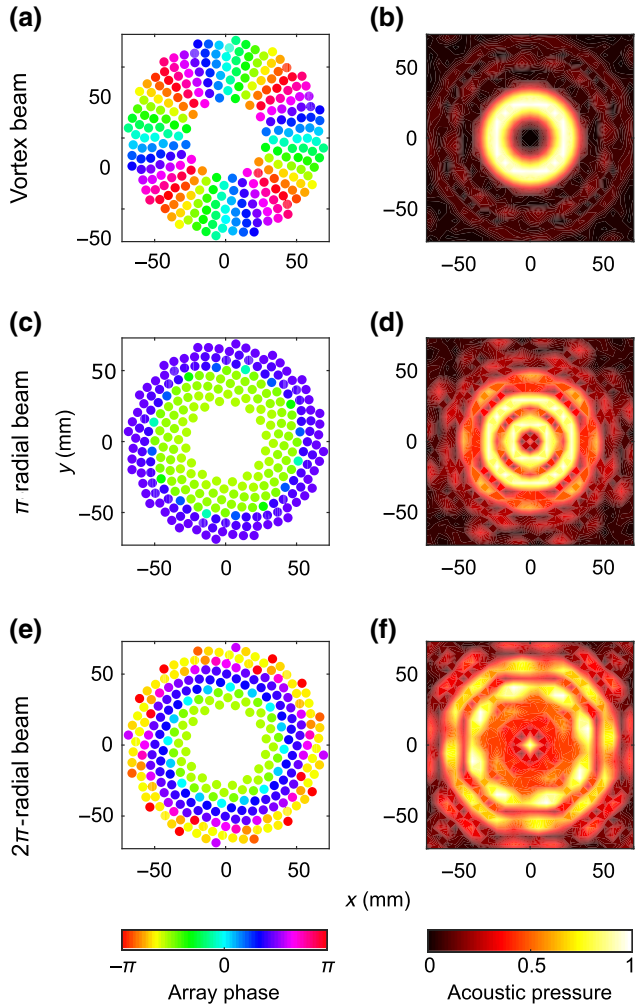

FIG. 2. Three acoustic beam shapes used for trapping spherical targets: vortex (a),(b), π radial (c),(d), and 2π-radial (e),(f) beams. On the left, the phase of each element in the array is shown, and on the right the pressure field created on the transverse plane at the focus is shown. A vortex beam of $M = 4$ topological charge is shown here for illustration. The array phase of a vortex beam (a) has circumferential variation, while the array phase for the π radial (c) and 2π-radial (e) beams vary along the radial direction. The normalized focal pressure (b),(d),(f) distribution in the x-y plane is shown for each case. Each beam creates in the focal plane a null and a ring of pressure with which to trap the sphere in the lateral direction while minimizing the axial radiation force.

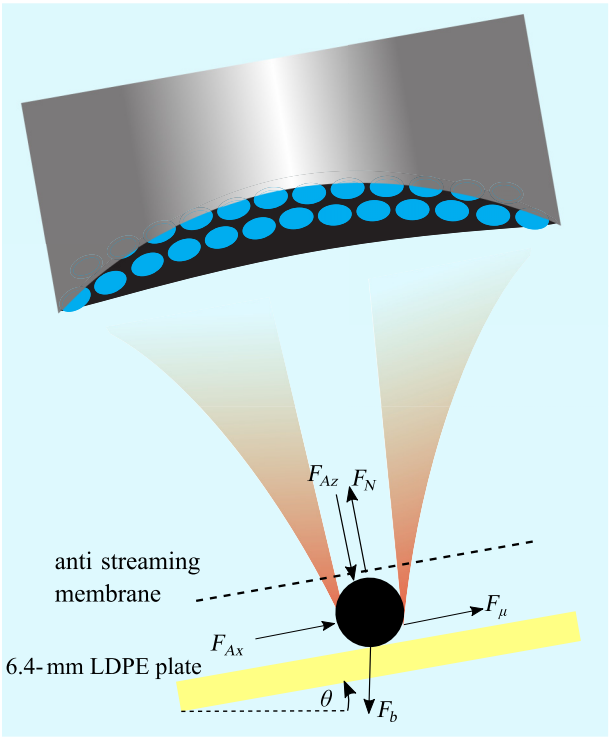

FIG. 3. Experimental setup showing the rotation of the frame-array combination until the spherical target rolls off at the angle of maximum total lateral force $\theta_{\max}$. The diagram represents the static equilibrium equation used to calculate the lateral acoustic radiation force from the measured angle $\theta_{\max}$. The coordinate system rotates with the array such that the x axis is parallel to the LDPE plate and the z axis coincides with the acoustic axis.

forces and $\theta_{\max}$ are related by the following force balance equation from Fig. 3

$$F_{Ax} = F_b \times (\sin\theta_{\max} - \mu\cos\theta_{\max}) - \mu F_{Az}, \qquad (1)$$

where the component of the buoyant weight F_b of the sphere parallel to the plate pulls the sphere from the trap but is resisted by the friction force F_μ acting with F_{Ax} to hold the sphere in place. The friction force is the product of the friction coefficient (measured as described below) and the normal force F_N, which is equal and opposite to the sum of F_{Az} and the normal component of the buoyant weight of the sphere F_b to the plate at angle θ. Additionally, a 10-μm, antistreaming membrane is placed 2–6 mm (depending on the sphere size) above the target sphere to prevent fluid flow caused by acoustic streaming from affecting the measurement. Additional measurements of the effect of an antistreaming membrane are reported in Appendix A. Additional hydrodynamic forces are negligible at such low rotational speeds. The Stokes drag force for a linear speed of 4 mm/s is calculated to be three orders of magnitude lower than the calculated lateral acoustic force [60] and is, therefore, neglected in all calculations.

Solid spheres made of glass, brass, and ceramic with sizes 2–6 mm are tested. The nominal sizes and acoustic properties of the tested spheres are described in Table I. The material properties in Table I are obtained from the suppliers (glass spheres from Propper Manufacturing Co., Inc., brass and ceramic from McMaster-Carr). Table I lists the elastic properties for each material type where ρ_s is the density of the sphere, and c_l and c_t are the longitudinal and shear wave speeds in the material, respectively. For vortex beams, two M values are tested for each sphere with widths

TABLE I. Physical characteristics of the spheres and the beam shapes used in the experiments.

Material	Glass					Ceramic	Brass
Elastic properties			$\rho_s = 2500$ g/cm^3 $c_l = 5448$ m/s $c_t = 3264$ m/s			$\rho_s = 3290$ g/cm^3 $c_l = 10\,851$ m/s $c_t = 6091$ m/s	$\rho_s = 8530$ g/cm^3 $c_l = 4842$ m/s $c_t = 2166$ m/s
Diameter (mm)	2	3	4	5	6	4.8	4.8
Beam shape	$2_\pm$, $3_\pm$, π radial	$3_\pm$, $4_\pm$	$4_\pm$, $5_\pm$, 2π-radial	$5_\pm$, $6_\pm$, 2π-radial	$6_\pm$, $7_\pm$	$4_\pm$, $5_\pm$	$4_\pm$, $5_\pm$

mostly near the beam diameter. However, since the beam width cannot be adjusted for the π and 2π-radial beams, only specific sphere diameters are tested. Since multiple sizes of the spheres are examined and tested under more than one trapping acoustic beam, results are presented as the ratio η of the sphere diameter to beam width, which is defined by the diameter of peak intensity within the inner ring of the acoustic field in the transverse focal plane. The value of η varies from 0.7 to 1.4, where a larger η denotes a narrow beam with respect to the sphere's diameter and vice versa.

The LDPE plate is well matched to water with a measured power reflection coefficient less than 1%, and therefore, minimally interferes with the incident acoustic beam. The friction coefficient μ of the three different sphere materials on LDPE is measured by recording the maximum angle θ_μ at which each sphere falls without any acoustic exposure: the relation is $\mu = \tan\theta_\mu$. This assumes an idealized friction model where a geometrically perfect nondeformable sphere in contact with a perfectly nondeformable flat surface at a single point of contact will roll with the application of a tangential force, as rolling of the sphere is observed during experiments. The friction coefficient is measured 10 times for every sphere, five in each direction. The mean and standard deviation of μ for all spheres with the same composition are measured to be 0.059 ± 0.024, 0.030 ± 0.009, and 0.022 ± 0.007 for glass, ceramic, and brass spheres. Using a μ measured for each individual sphere rather than for each composition might have improved precision and accuracy at the loss of generality, but this was not tested.

For each sphere, the acoustic power is varied to ensure that the sphere falls at an angle $\theta_{\max}$ between 20° and 80°. These variations are aimed to avoid uncertainty in force for smaller angles and null results when the sphere does not fall at large angles. The acoustic power of the array is low enough to ensure negligible nonlinear acoustic propagation effects and minimal heating of the plastic. In all settings, the second harmonic amplitude is <1% of the fundamental amplitude. The output is pulsed, and the time-averaged acoustic power is 1.6–12.9 W, adjusted by changing the pulsing duty cycle (10%–86%). Such low focal pressures relative to the intended use for which this array is designed [55] require that the minimum operating voltage is used, and power is adjusted by controlling the length of pulses to change the duty cycle. Since theory calculates forces from continuous acoustic waves, time-averaged values are used to account for pulsing in the experiment.

An alternating pulsing scheme is used to prevent the spheres trapped by vortex beams from spinning. Vortex beams have an angular momentum component [61–66] caused by their helical wavefront [26,61,67,68]. This angular momentum causes rotational instabilities leading to the ejection of spheres from the trap. Since the radiation force and torque are time-averaged quantities, the torque is eliminated by delivering two consecutive vortex pulses of equal duration with opposite helicity and the same topological charge magnitude (i.e., $\pm M$) [39,69,70], which we denote as $M_\pm$. The pulse duration is set to 661 μs, which is shorter than the minimum acceleration time, $\tau = I/8\pi a^3\rho\nu$, needed for a fully absorbing sphere to reach a terminal angular velocity due to drag torque, where I and a are the moment of inertia and radius of the sphere, and ν is the kinematic viscosity of the medium [39,64].

The measured angles and forces are compared to the calculated angles and forces. The angle is measured directly while the forces are calculated from the measured angles using Eq. (1). The axial acoustic radiation force F_{Az} is found from simulation then scaled to match the applied acoustic power of the experiment by multiplying by the ratio of the time-average applied, acoustic power to the theoretical power. The linear relationship between acoustic power and radiation force is examined and verified as reported in Appendix B. The simulated acoustic radiation forces of each measurement are calculated based on the density of and sound speed in water, and the water temperature is maintained within 0.5 °C. Reported measured angles are the average of 10 measurements: five rotations of the experiment in the clockwise direction and five in the counterclockwise direction alternating. Measured data are shown as mean and standard deviation. The discrepancy between the measured and calculated values is determined using the following equation

$$D = |\chi_m - \chi_{\text{th}}|/\chi_{\text{th}} \times 100\%, \tag{2}$$

where χ_m and χ_{th} are the measured and theoretical quantities of interest.

C. Manipulation of objects

To demonstrate the stable positional control of large solid objects, a 5-mm glass sphere is steered along a

preprogrammed, two-dimensional (2D) path on a flat, LDPE sheet positioned perpendicular to the beam axis. To dynamically steer the focus along a desired path, the phase delay on each element of the array is found by calculating the difference between the distance from the element center on the array's surface and the desired location as referenced to the geometrical focus of the array. The element's phase ϕ to synthesize and to steer an acoustic trap along a preprogrammed path is defined by superimposing the phase required to synthesize the trap on the phase delay to steer the focus. The 5-mm, glass sphere is trapped by a $M_{\pm} = 6$ vortex and steered along a specified path with the preprogrammed phase of each element i defined at location p as follows:

$$\phi_i = M \times \arctan\left(\frac{x_{i2}}{x_{i1}}\right) + \left[R - \sum_{j=1}^{3}\sqrt{(x_{ij} - p_j)^2}\right] \times k, \tag{3}$$

where ϕ_i is the phase delay on element i, R is the radius of curvature of the array, x_{ij} is the x_j coordinate of element i, p_j is the j coordinate of point p along the desired steering path, and k is the wave number. The sphere is steered along a three-leaf polar path represented by the following equation

$$r(\varphi) = r_0 \cos(3\varphi), \tag{4}$$

where $r_0 = 13$ mm, r is the radial distance in millimeters, and φ is the angular location in radians. The sphere is steered with an average speed of 6 mm/s. A camera is positioned with its viewing axis parallel to the acoustic axis to record the motion. The array is operating at 50% duty cycle with a time-averaged acoustic power of 7.5 W. The desired path and the measured path of the sphere centroid are compared, and the difference reported as discrepancy in radial distance as defined in Eq. (2) above.

III. RESULTS AND DISCUSSION

A. Theoretical model

Simulation results for the lateral and axial acoustic radiation forces are used in the validation of the force measurements. Figure 4 shows the calculation of the acoustic radiation forces on a 4-mm, glass sphere at all locations in the focal x-y plane by all three beams. The axial component of the acoustic radiation force F_{Az} reaches a local minimum inside the acoustic ring. There is negligible acoustic radiation force in the y direction along the x axis because of the averaging of the acoustic forces produced by $+M$ and $-M$. The solid dot marks the location of the centroid of the sphere when we measure the maximum lateral acoustic force F_{Ax}. This location indicates the F_{Az} value used in the friction calculation in Eq. (1). Beyond this location, the sphere falls.

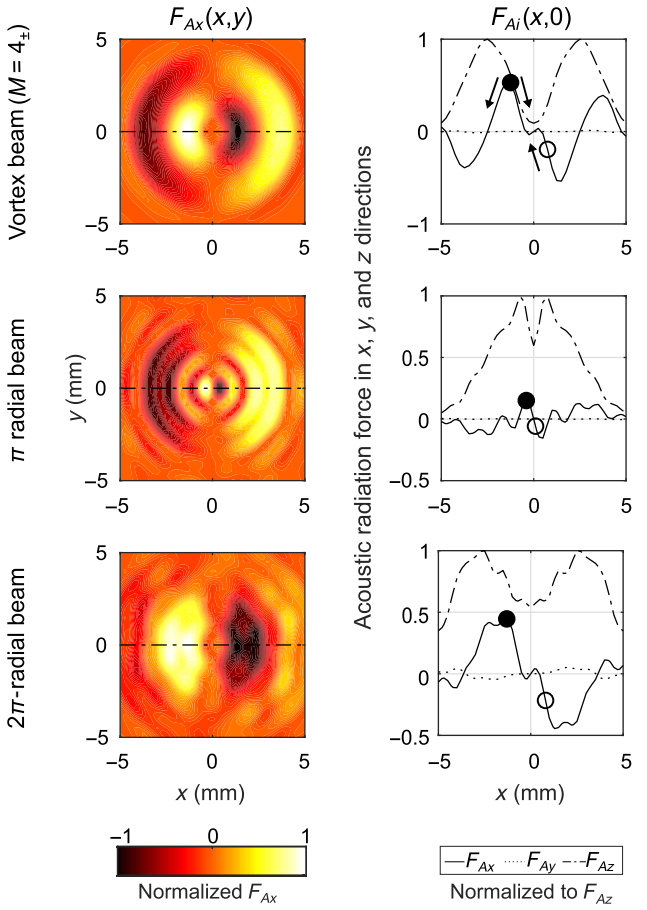

FIG. 4. Simulation of the lateral acoustic radiation force F_{Ax} normalized to its maximum on a 4-mm glass sphere throughout the focal x-y plane for the three beams (left column). F_{Ax} for a vortex beam is the average of the force produced by alternating $M = 4, -4$. Within the visible rings, all beams create a positive F_{Ax} (light color) on the left, which pushes the sphere to the right, and a negative F_{Ax} on the right, which pushes the sphere to the left. In the center without any asymmetry in other forces, the net lateral acoustic radiation force holds the sphere in place effectively trapping it. The right column displays the acoustic radiation forces F_{Ax}, F_{Ay}, and F_{Az} normalized to the maximum F_{Az} value at different sphere locations along the x axis (the dashed line of the left column). The open and solid dots show centroid positions of the 4-mm sphere within the trap. With the rotation of the array-platform system, because of an increasing effect of gravity with slope, the sphere will roll from the location of the open dot to the location of the solid dot, which is the position of maximum lateral acoustic force that is pushing to the right in this case. Further increase in angle will cause the sphere to fall from the trap.

B. Lateral force measurements

Measurements of the angle of maximum total lateral force $\theta_{\max}$ for the spherical targets of different sizes and compositions are compared to the calculations found from the forces calculated with the SB model and Eq. (1). The plot in Fig. 5 compares calculated and experimental values

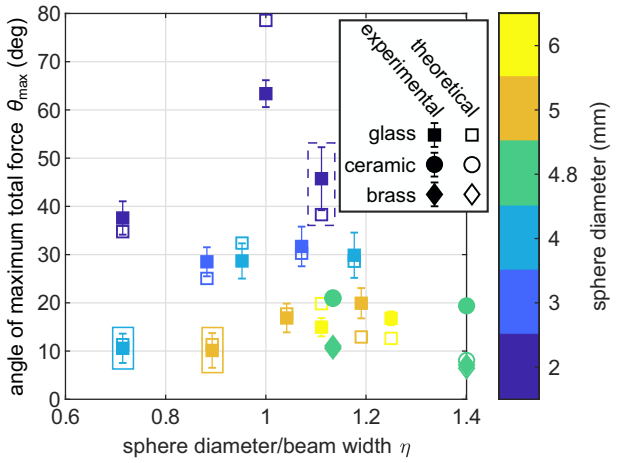

FIG. 5. Comparison between the measured and calculated predicted angle θ_{max} versus the ratio of sphere diameter to beam width η. Experimental data are the mean and error bars show the standard deviation of 10 replicate measurements. Close proximity of solid and open marks shows the good agreement between measurement and theory over a range of sphere sizes and compositions. Different compositions are denoted by different data point shapes. Data point pairs within the dashed rectangle are for the π radial beam and within the solid rectangle are for the 2π-radial beam, both of which have a fixed beam width. Sphere diameters are shown by color, and M is adjusted to alter the beam width and create the η displayed. Overall calculations with the SB model compare well to measurement for different beams, sphere diameters, and sphere compositions.

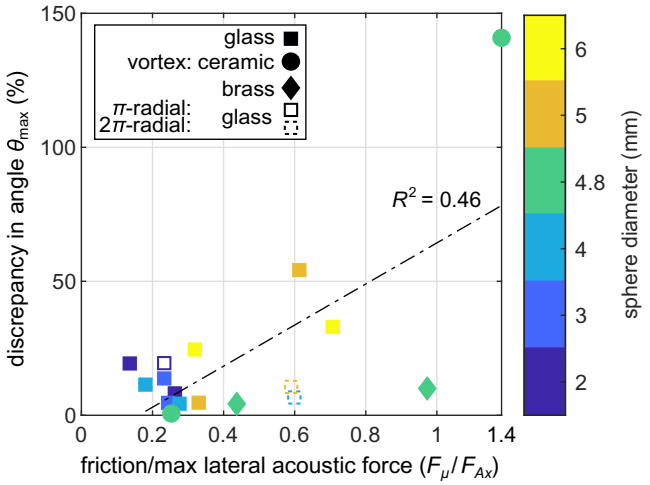

FIG. 6. Discrepancy between calculated and measured angles plotted versus the ratio of friction to theoretical maximum lateral acoustic force. The discrepancy in angle is $21.8 \pm 32.4\%$ on average, and agreement is good. There appears to be a correlation between the discrepancy and the friction component suggesting the error in friction is a factor in the discrepancy although the correlation is weak.

of data pairs. Good agreement between measured and calculated θ_{max} is found for multiple beams, targets sizes, and targets compositions (Fig. 5). The successful trapping of spheres that are 40% larger than the beam width ($\eta = 1.4$) is demonstrated.

Examination of Fig. 5 shows two cases of interest where theory and experiment diverge. First, theoretical prediction for the 2-mm, glass sphere at $\eta = 1.0$ is 14° larger than the measured angle. This translates to a discrepancy of 19.34% in θ_{max} or 11.73% in F_{Ax}. This case has the lightest sphere, the lowest duty cycle (acoustic power), and the highest angle of 63°. We attribute the large discrepancy to the low duty cycle of 10.5% and hypothesize that the sphere moves between pulses under gravity. Under this condition, the sphere would fall approximately 0.55 mm (greater than half the radius) between pulses, which is sufficient to move the sphere from a stable to unstable position in the beam (see Appendix B for the values of duty cycle and time-averaged power used). Using pulses rather than continuous exposure may have affected other spheres to a lesser degree especially when the beam was narrow compared to the sphere diameter and the sphere had only a short distance to escape the trap. However, the fact the discrepancy could be greater or less than measurement without any observed trend does not support a general effect of pulsing. The measurement with the 4.8-mm, ceramic sphere at $\eta = 1.4$ also diverges from the theoretical prediction and is described in more detail below.

The discrepancies between measurements and theoretical predictions are calculated according to Eq. (2) for each sphere composition and size under the acoustic force of a specific beam. Discrepancies in angle θ_{max} are potted versus the theoretical ratio of the total friction force, caused by buoyancy and F_{Az}, to the maximum lateral acoustic force F_{Ax} in Fig. 6. Overall, the average discrepancy is $21.8 \pm 32.4\%$ in θ_{max} and $32.8 \pm 58.1\%$ in F_{Ax}. There is good agreement between measurement and theory, particularly when the ratio of F_μ/F_{Ax} is ≤ 0.6, where the average discrepancy is $10.2 \pm 7.2\%$ in θ_{max} and $11.7 \pm 8.3\%$ in F_{Ax}. A potential source of discrepancy is the uncertainty with friction, which increases discrepancy as friction becomes a more significant component of the forces. A linear fit to the error has a slope of 76.6% / (F_μ/F_{Ax}) but a weak correlation of $R^2 = 0.46$.

The discrepancy between measurement and theory is small considering the uncertainties in μ, medium acoustic properties, sphere size, and acoustic properties, and the variance in the acoustic power output of the array. For instance, the variation in the diameters of the spheres per the manufacturers' specifications is between 5% and 10% for large to small spheres, respectively. The measured variations in water temperature of <1 °C have negligible effect on the calculated F_{Ax} and θ_{max}. Also, the driving electronics supplies power with a $\pm 2.5\%$ uncertainty. As discussed above, the simulation assumes a continuous

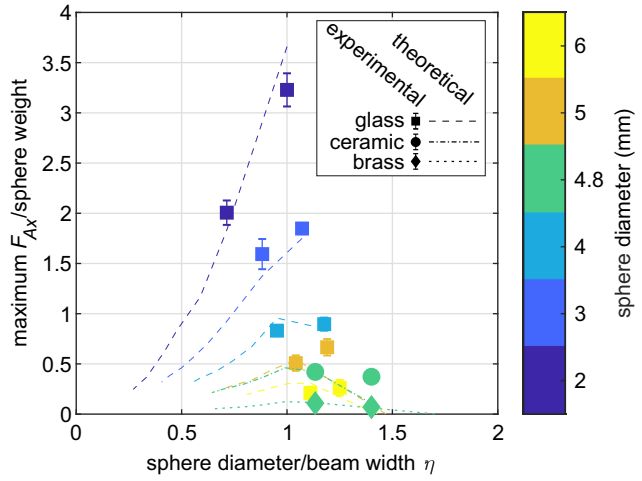

FIG. 7. Ratio of maximum lateral acoustic force F_{Ax} to sphere weight in a 10-W vortex beam versus the ratio of sphere diameter to beam width η. Theoretical lines connect a few discrete values calculated for discrete values of M, and therefore, discrete beam widths for a specific sphere diameter and composition. Theoretical lines are also truncated where there is no lateral acoustic radiation force as the sphere is too large. Regardless of the sphere material, the most efficient trapping occurs at η close to 1.

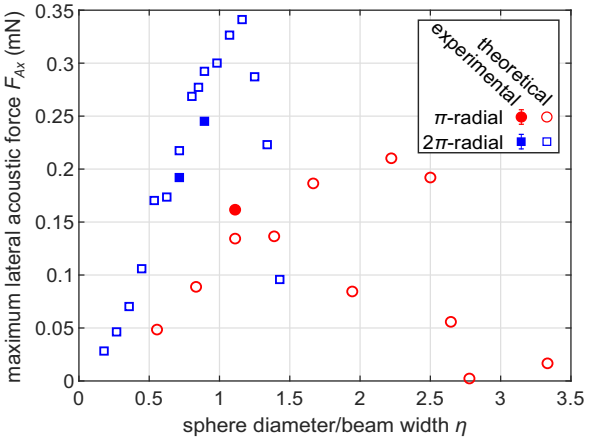

FIG. 8. Maximum lateral acoustic force F_{Ax} of 10-W π and 2π radially varying phase beams versus the ratio of the sphere diameter to beam width η. F_{Ax} diminishes for small or large η. The π radial beam rings have the same acoustic intensity, and both can trap spheres as F_{Ax} reaches a maximum close to $\eta = 1$ and 2. The 2π-radial follows a smoother shape where maximum F_{Ax} is centered at $\eta \approx 1$, since the inner ring has higher intensity and is the effective trapping ring.

acoustic exposure, and the array is operated by transmitting pulses. Appendix B shows the agreement in acoustic power between the experimental pulsed exposure and the equivalent simulated continuous exposure.

The lateral acoustic radiation force of varying vortex beams (different $M_{\pm}$) for a given sphere diameter and composition is calculated directly with the SB model then compared to the lateral force calculated from the measured angle $\theta_{\max}$ with Eq. (1). Figure 7 shows the ratio of F_{Ax} from a 10-W beam to the weight of the sphere with buoyancy neglected, which is sphere mass m times the gravitational acceleration g. Each line connects calculations at discrete $M_{\pm}$, while experimental values are shown at two different $M_{\pm}$ for each sphere. The maximum F_{Ax} occurs when the sphere diameter and beam width are equal, regardless of the material. In many cases, a vortex with a very small or large topological charge integer produces no trapping force in simulation, which is indicated by the absence of the continuity of the theoretical lines. At 10-W acoustic power, F_{Ax} is close to 3.5 times the weight of a 2-mm, glass sphere (a mass of 46 mg) and is on the order of the weight of the largest spheres in this study. The array and power supply can produce up to 1200 W, and as noted in the Methods, the lowest operating voltage setting is used and adjusted by further reducing the duty cycle. Thus, only a small fraction of the available power of the array is needed to create lateral force equal to the weight of the spheres.

A similar analysis to Fig. 7 is carried out for the π radial and 2π-radial beams at 10 W and shown in Fig. 8. Since these beams have a fixed width, only specific sphere diameters are used in the measurements as opposed to the vortex beams where M is changed to adjust the beam width to the sphere. For calculations in Fig. 8, the sphere diameter varies for each point, while the beam width remains constant. Figure 8 shows the lateral acoustic radiation force versus η. Generally, F_{Ax} follows the same trend in Fig. 7 where it is highest near $\eta = 1$, and vanishes as the sphere is much smaller or larger compared to beam width; however, because of the multiple ring structure, the behavior is more complex due to contribution from both rings. For the 2π-radial beam, where the inner ring is stronger than the outer ring, the highest acoustic force is centered around $\eta = 1$, as is the case for the vortex beam. For the π radial beam, where both rings are of equal intensity, we see a bimodal behavior where the sphere is trapped by the ring closest to its diameter. Simulations show that 2.5 and 3 mm glass spheres are in a transition region as they are trapped by both rings, whereas a 2-mm sphere is trapped primarily by the inner ring, and a 3.5-mm sphere is trapped by the outer ring. Video 1 shows the simulation for the 2.5-mm sphere.

C. Manipulation of objects

The use of a vortex beam to steer a large solid object is tested. Video 2 shows superimposed select frames of the red, 5-mm, glass sphere moving along the programmed path over a plane perpendicular to the acoustic axis. The measured locations of the center of the sphere from each frame of the movie of one complete path are plotted over the intended path in Fig. 9(a). Figure 9(b) shows the average discrepancy in radius between the measured and the

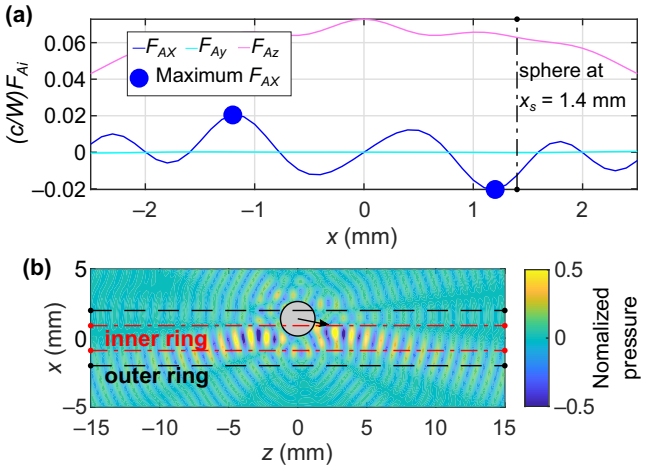

VIDEO 1. Simulation of a 2.5-mm glass sphere in the acoustic field of the π radial beam. This beam has two trapping rings of equal intensity. For a sphere this size and composition, both rings contribute to the trapping. The acoustic force components F_{Ai} are shown at each location along the x axis (a) and are nondimensionalized by a factor of c/W, where c is the sound speed in water and W is the acoustic power of the beam. Locations of the maximum lateral acoustic force F_{Ax} on each side of the trapping ring are marked by a solid blue dot. The wave propagates from left to right incident on the sphere located at $x_s = 1.4$ mm, and the resulting normalized scattered pressure field is shown (b). A black arrow originating from the center of the sphere indicates the direction of the force. Both the inner and outer rings indicated by dotted red and dashed black lines contribute to the trapping of spheres with diameters ranging from 2.5 to 3 mm in the region between $|x| \geq 0.9$ mm and $|x| \leq 1.5$ mm, which can be seen from the scattering of the incident pressure field away from the acoustic axis and the resulting force direction toward the axis. Additionally, spheres smaller than 2.5 mm are predominantly trapped by the inner ring while spheres larger than 3 mm are trapped by the outer ring.

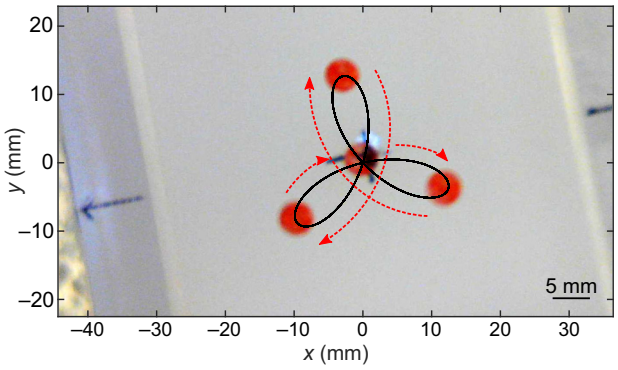

VIDEO 2. Superimposition of select frames of the trapping and dynamic steering by a $M = 6_{\pm}$ vortex beam of a 5-mm glass sphere over a path defined by Eq. (4), where the targets starts at the center, then moves to the right and follows the red arrows around each petal and back to the center. The view is from a camera mounted in the center of the array, such that both are facing down the acoustic axis toward the sphere.

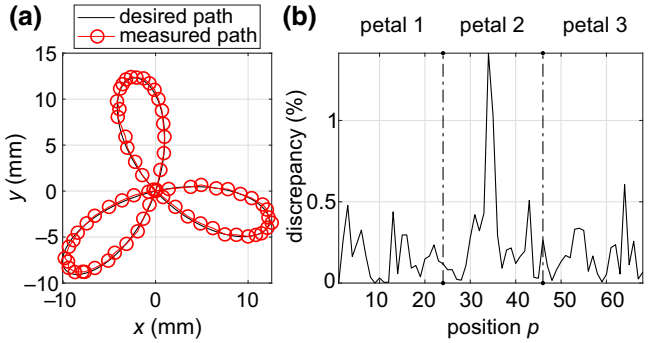

FIG. 9. Analysis of the dynamic steering of a 5-mm glass sphere from Video 2 over a path defined by Eq. (4). Good agreement is shown in (a) between the theoretical path (black line) and measured path (shown as open dots drawn around the center of the sphere from every frame of the video). The discrepancy in radius is shown in (b) between the measured and intended motion plotted versus each programmed position of the path as defined in Eq. (4).

intended paths at each position along the preprogrammed path. The maximum and overall mean errors from the intended path are 1.41% and 0.20 ± 0.23% corresponding to a maximum and mean absolute difference of 0.58 mm and 0.15 ± 0.010 mm. The largest deviation occurs at the outermost tip of each petal. Two factors may influence the discrepancy here: the tip of the petal causes the highest acceleration because of the curvature of the path, and the beam is weaker and less focused further off axis. Nevertheless, the mean absolute difference along the path is less than 1/5 of a wavelength.

IV. CONCLUSTION

In this study, successful lateral trapping of dense elastic spheres ranging in sizes from 2λ to 6λ by different beams is demonstrated in water. The lateral trapping forces of vortex beams and two additional synthesized beams on large objects are measured. Capability of the beams to trap spheres 40% larger than the beam width is achieved by transmitting equal-duration vortex pulses of opposite helicity. An important metric for the trapping strength is defined as the geometric ratio of sphere diameter to beam width η. It is shown that maximum trapping strength occurs for any sphere composition when the value of η is close to unity. The lateral acoustic radiation force is on the order of the weight of the spheres used in this study for a 10-W acoustic beam. The measured lateral acoustic radiation forces are compared to the theoretical predictions, and good agreement is shown for different beams, sphere diameters, and sphere compositions. Acoustic steering of spheres on a flat surface is demonstrated in water with high accuracy. Quantitative verification of the theoretical

model along with the experimental realization of acoustically induced lateral trapping and steering of objects on the same order of or larger than the wavelength and having arbitrary elastic properties, lays the groundwork for the development of acoustic manipulation of large objects for various physical, biological, and medical applications.

ACKNOWLEDGMENTS

The authors would like to thank our collaborators at the Center for Industrial and Medical Ultrasound at the University of Washington. In particular, we would like to thank Bryan Cunitz for help programming the Verasonics instrument and Brian MacConaghy for help in fabricating parts of the experiment. This work was supported by the National Institutes of Health NIDDK Grants No. P01-DK043881 and No. K01-DK104854, and NIBIB Grants No. R01-EB007643 and No. RFBR 17-02-00261.

APPENDIX A: ACOUSTIC STREAMING

Acoustic streaming is the fluid motion caused by absorption of the wave momentum by the surrounding fluid. Streaming increases with acoustic power and uninterrupted propagation length through the fluid. The resulting fluid motion can affect the stability of the target and the force measurement. To ensure the accuracy of the force measurements, the influence of acoustic streaming is investigated at low- and high-power levels, and with and without an acoustically transparent barrier in place. A 5-mm, glass sphere is trapped by a $M = 6_{\pm}$ vortex, then the angle of maximum total lateral force is measured for three configurations: no antistreaming membrane, an elevated membrane positioned 2 cm above the sphere, and an antistreaming membrane positioned 6 mm above the sphere. The three configurations are tested using low- and high-power levels of 3.3 and 8.7 W by increasing the pulse duration or duty cycle. Figure 10 shows $\theta_{\max}$ for each power level versus the three membrane configurations. A mean of the variance (ANOVA) test is used to compare the mean in $\theta_{\max}$ among the configurations at each power level. The test results yield p values of 0.89 and 0.93 at power levels of 3.3 and 8.7 W, which indicates there is no statistical difference among the configurations at each power level. Therefore, acoustic streaming has minimal effect on the accuracy of the measurements and the membrane is an unnecessary precaution.

APPENDIX B: ACOUSTIC RADIATION FORCE LINEARITY WITH ACOUSTIC POWER

In the lateral force measurement experiment, the time-averaged acoustic power used for every sphere is changed to ensure an angle of maximum total lateral force $\theta_{\max}$ between 20° and 80°. Therefore, to control the acoustic power delivered the duty cycle is tuned for each sphere as per Table II.

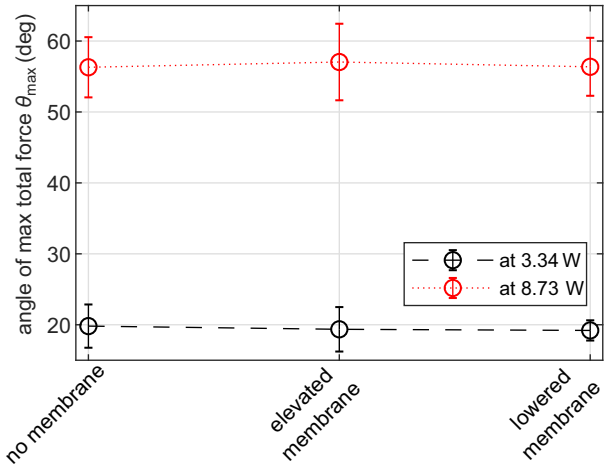

FIG. 10. Effect of acoustic streaming on the lateral trapping force measurement at two different power levels of 3.3 and 8.7 W versus three different antistreaming membrane configurations. The angle of maximum total lateral force for a 5-mm glass sphere does not significantly vary among configurations at either power level, which demonstrates the absence of acoustic streaming effects in the measurements.

Furthermore, theoretically, acoustic radiation force is linearly proportional to the acoustic power. For instance, the force acting on a fully absorbing target, $F_A = W/c$ [12], where F_A is the acoustic radiation force, c is the speed of sound, and W is the acoustic power. A deviation from the linear relationship between the radiation force and acoustic power could serve as an indication of measurement artifacts (such as acoustic streaming, nonlinear effects in acoustic propagation, or incorrect measurement of the source power), which should be avoided. To verify the linear relationship and the scaling of the theoretical simulation to experimental results and vice versa based on the power ratio, a 5-mm, glass sphere is trapped by a $M = 6_{\pm}$ vortex beam, and the angle of maximum total lateral force $\theta_{\max}$ is recorded as a function of power output from the array. By reordering Eq. (1) and defining, similar to the approach in Ref. [47], a nondimensional coefficient γ_i, where $\gamma_i = (c/W)F_{Ai}$ is proportional to the acoustic force component F_{Ai}, Eq. (1) can be written as a function of W and γ_i as follows:

$$\sin\theta - \mu\cos\theta = (\gamma_x + \mu\gamma_z) \times \frac{W}{cF_b}. \tag{B1}$$

When the acoustic power is zero in the experiment, there is a nonzero $\theta_{\max}$ due to friction. Therefore, the equilibrium equation is rearranged to be in the form of Eq. (B1) by subtracting $\mu\cos\theta$ from the left-hand side in order to have a zero value at no acoustic exposure.

TABLE II. The duty cycle and equivalent time-averaged acoustic power for each measurement point.

Material	Glass					Ceramic			Brass	
Diameter (mm)	2		3	4	5	6	4.8	5	4.8	5
Beam shape	$2_{\pm}$, $3_{\pm}$	π-radial	$3_{\pm}$, $4_{\pm}$	$4_{\pm}$, $5_{\pm}$, 2π-radial	$5_{\pm}$, $6_{\pm}$	2π-radial	$4_{\pm}$, $5_{\pm}$	$5_{\pm}$	$5_{\pm}$	$5_{\pm}$
Duty cycle	10.50%	16.20%	10.50%	19.20%	22.00%	28.60%	35.30%	58.10%	85.70%	
time-averaged acoustic power	1.6	2.4	1.6	2.9	3.3	4.3	5.3	8.7	12.9	

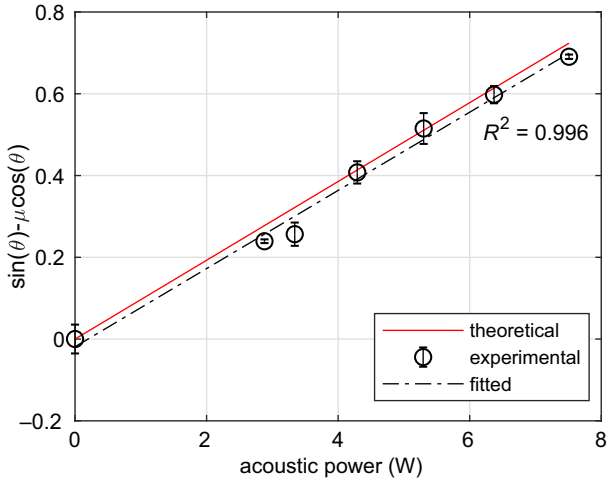

FIG. 11. Relationship between the acoustic power W and nondimensionalized factor corresponding to the acoustic radiation forces represented in terms of the angle of maximum total lateral force. Experimental data [open circles with error bars indicating standard deviation ($N = 10$)] show agreement with theoretical (solid line) estimates of the angle of maximum total lateral force. A best-fit line (dashed line) with a high correlation coefficient of $R^2 = 0.996$ indicates good linearity of the measured data points.

Experimental data points are acquired as $\theta_{\max}$ vs W, while the theoretical angle predictions are calculated using Eq. (1) at the same W for comparison. The experimental time-averaged power is used to compare the results to their corresponding theoretical acoustic power.

The theoretical line and experimental data points from Eq. (B1) are shown in Fig. 11 along with the best-fit line to the measured data. The best-fit line has a slope of 0.0956 per watt and a strong correlation of $R^2 = 0.996$. Therefore, the acoustic radiation force is linear in the range of the acoustic power applied and the time-averaged measured power is equivalent to the calculated estimate continuous power exposure.

[1] A. Ashkin, Acceleration and Trapping of Particles By Radiation Pressure, Phys. Rev. Lett. **24**, 156 (1970).

[2] A. Ashkin, J. M. Dziedzic, J. E. Bjorkholm, and S. Chu, Observation of a single-beam gradient force optical trap for dielectric particles, Opt. Lett. **11**, 288 (1986).

[3] A. Ashkin, J. M. Dziedzic, and T. Yamane, Optical trapping and manipulation of single cells using infrared laser beams, Nature **330**, 769 (1987).

[4] P. Jing, J. Wu, G. W. Liu, E. G. Keeler, S. H. Pun, and L. Y. Lin, Photonic crystal optical tweezers with high efficiency for live biological samples and viability characterization, Sci. Rep. **6**, 1 (2016).

[5] M. D. Wang, H. Yin, R. Landick, J. Gelles, and S. M. Block, Stretching DNA with optical tweezers, Biophys. J. **72**, 1335 (1997).

[6] S. Chu, J. E. Bjorkholm, A. Ashkin, and A. Cable, Experimental Observation of Optically Trapped Atoms, Phys. Rev. Lett. **57**, 314 (1986).

[7] S. Chu, Laser manipulation of atoms and particles, Science **253**, 861 (1991).

[8] J. Ye, H. J. Kimble, and H. Katori, Quantum state engineering and precision metrology using state-insensitive light traps, Science **320**, 1734 (2008).

[9] Lord Rayleigh, On the pressure of vibrations, London, Edinburgh, Dublin Philos. Mag. J. Sci. **3**, 338 (1902).

[10] L. V. King, On the acoustic radiation pressure on spheres, Proc. R. Soc. London. Ser. A - Math. Phys. Sci. **147**, 212 LP (1934).

[11] P. J. Westervelt, The theory of steady forces caused by sound waves, J. Acoust. Soc. Am. **23**, 312 (1951).

[12] P. J. Westervelt, Acoustic radiation pressure, J. Acoust. Soc. Am. **26**, 1 (1957).

[13] D. Foresti, M. Nabavi, M. Klingauf, A. Ferrari, and D. Poulikakos, Acoustophoretic contactless transport and handling of matter in air, Proc. Natl. Acad. Sci. **110**, 12549 (2013).

[14] Y. Ochiai, T. Hoshi, and J. Rekimoto, Pixie Dust : graphics generated by levitated and animated objects in computational acoustic-potential field, ACM Trans. Graph. **33**, Article 85 (2014).

[15] A. Marzo, S. A. Seah, B. W. Drinkwater, D. R. Sahoo, B. Long, and S. Subramanian, Holographic acoustic elements for manipulation of levitated objects, Nat. Commun. **6**, 8661 (2015).

[16] C. R. P. Courtney, B. W. Drinkwater, C. E. M. Demore, S. Cochran, A. Grinenko, and P. D. Wilcox, Dexterous manipulation of microparticles using Bessel-function acoustic pressure fields, Appl. Phys. Lett. **102**, 123508 (2013).

[17] D. Baresch, J. Thomas, and R. Marchiano, Observation of a Single-Beam Gradient Force Acoustical Trap for Elastic Particles : Acoustical Tweezers, Phys. Rev. Lett. **116**, 1 (2016).

[18] T. Laurell, F. Petersson, and A. Nilsson, Chip integrated strategies for acoustic separation and manipulation of cells and particles, Chem. Soc. Rev. **36**, 492 (2007).

[19] X. Ding, S.-C. S. Lin, B. Kiraly, H. Yue, S. Li, I.-K. Chiang, J. Shi, S. J. Benkovic, and T. J. Huang, On-chip manipulation of single microparticles, cells, and organisms using surface acoustic waves, Proc. Natl. Acad. Sci. **109**, 11105 (2012).

[20] M. J. Shortencarier, P. A. Dayton, S. H. Bloch, P. A. Schumann, T. O. Matsunaga, K. W. Ferrara, and S. Member, A method for radiation-force localized drug delivery using gas-filled lipospheres, IEEE Trans. Ultrason. Ferroelectr. Freq. Control. **51**, 822 (2004).

[21] L. P. Gor'kov, On the forces acting on a small particle in an acoustical field in an ideal fluid, Sov. Phys. **6**, 315 (1962).

[22] P. Glynne-Jones, C. E. M. Démoré, C. Ye, Y. Qiu, S. Cochran, and M. Hill, Array-controlled ultrasonic manipulation of particles in planar acoustic resonator, IEEE Trans. Ultrason. Ferroelectr. Freq. Control. **59**, 1258 (2012).

[23] W. T. Coakley, D. W. Bardsley, M. A. Grundy, F. Zamani, and D. J. Clarke, Cell manipulation in ultrasonic standing wave fields, J. Chem. Technol. Biotechnol. **44**, 43 (1989).

[24] J. J. Hawkes, D. Barrow, and W. T. Coakley, Microparticle manipulation in millimetre scale ultrasonic standing wave chambers, Ultrasonics **36**, 925 (1998).

[25] C. A. Cain and S. Umemura, Concentric-ring and sector-vortex phased-array applicators for ultrasound hyperthermia, IEEE Trans. Microw. Theory Tech. **34**, 542 (1986).

[26] B. Hefner and P. Marston, An acoustical helicoidal wave transducer with applications for the alignment of ultrasonic and underwater systems, J. Acoust. Soc. Am. **106**, 3313 (1999).

[27] D. Baresch, J. L. Thomas, and R. Marchiano, Spherical vortex beams of high radial degree for enhanced single-beam tweezers, J. Appl. Phys. **113**, 1 (2013).

[28] P. L. Marston, Axial radiation force of a Bessel beam on a sphere and direction reversal of the force, J. Acoust. Soc. Am. **120**, 3518 (2006).

[29] P. L. Marston, Radiation force of a helicoidal Bessel beam on a sphere, J. Acoust. Soc. Am. **125**, 3539 (2009).

[30] F. G. Mitri, Langevin acoustic radiation force of a high-order bessel beam on a rigid sphere, IEEE Trans. Ultrason. Ferroelectr. Freq. Control. **56**, 1059 (2009).

[31] P. L. Marston, Negative axial radiation forces on solid spheres and shells in a Bessel beam, J. Acoust. Soc. Am. **122**, 3162 (2007).

[32] F. G. Mitri, Negative axial radiation force on a fluid and elastic spheres illuminated by a high-order Bessel beam of progressive waves, J. Phys. A Math. Theor. **42**, 245202 (2009).

[33] A. Marzo and B. W. Drinkwater, Holographic acoustic tweezers, Proc. Natl. Acad. Sci. **116**, 84 (2018).

[34] M. A. B. Andrade, N. Pérez, and J. C. Adamowski, Particle manipulation by a non-resonant acoustic levitator, Appl. Phys. Lett. **106**, 1 (2015).

[35] J. Lee, K. Ha, and K. K. Shung, A theoretical study of the feasibility of acoustical tweezers: Ray acoustics approach, J. Acoust. Soc. Am. **117**, 3273 (2005).

[36] J. Lee and K. K. Shung, Radiation forces exerted on arbitrarily located sphere by acoustic tweezer, J. Acoust. Soc. Am. **120**, 1084 (2006).

[37] J. Lee, S. Y. Teh, A. Lee, H. H. Kim, C. Lee, and K. K. Shung, Single beam acoustic trapping, Appl. Phys. Lett. **95**, 21 (2009).

[38] K. H. Lam, H. S. Hsu, Y. Li, C. Lee, A. Lin, Q. Zhou, E. S. Kim, and K. K. Shung, Ultrahigh frequency lensless ultrasonic transducers for acoustic tweezers application, Biotechnol. Bioeng. **110**, 881 (2013).

[39] A. Marzo, M. Caleap, and B. W. Drinkwater, Acoustic Virtual Vortices with Tunable Orbital Angular Momentum for Trapping of Mie Particles, Phys. Rev. Lett. **120**, 44301 (2018).

[40] G. Maidanik and P. J. Westervelt, Acoustical radiation pressure due to incident plane progressive waves on spherical objects, J. Acoust. Soc. Am. **29**, 936 (1957).

[41] T. Hasegawa and K. Yosioka, Acoustic-radiation force on a solid elastic sphere, J. Acoust. Soc. Am. **46**, 1139 (1969).

[42] L. Zhang and P. L. Marston, Geometrical interpretation of negative radiation forces of acoustical Bessel beams on spheres, Phys. Rev. E - Stat. Nonlinear, Soft Matter Phys. **84**, 1 (2011).

[43] L. Zhang and P. L. Marston, Axial radiation force exerted by general non-diffracting beams, J. Acoust. Soc. Am. **131**, EL329 (2012).
[44] G. T. Silva, Off-axis scattering of an ultrasound bessel beam by a sphere, IEEE Trans. Ultrason. Ferroelectr. Freq. Control. **58**, 298 (2011).
[45] F. G. Mitri and G. T. Silva, Off-axial acoustic scattering of a high-order Bessel vortex beam by a rigid sphere, Wave Motion. **48**, 392 (2011).
[46] G. T. Silva, J. H. Lopes, and F. G. Mitri, Off-axial acoustic radiation force of repulsor and tractor bessel beams on a sphere, IEEE Trans. Ultrason. Ferroelectr. Freq. Control. **60**, 1207 (2013).
[47] O. A. Sapozhnikov and M. R. Bailey, Radiation force of an arbitrary acoustic beam on an elastic sphere in a fluid, J. Acoust. Soc. Am. **133**, 661 (2013).
[48] D. Baresch, J. L. Thomas, and R. Marchiano, Three-dimensional acoustic radiation force on an arbitrarily located elastic sphere, J. Acoust. Soc. Am. **133**, 25 (2013).
[49] T. S. Jerome, Y. A. Ilinskii, E. A. Zabolotskaya, and M. F. Hamilton, Born approximation of acoustic radiation force and torque on soft objects of arbitrary shape, J. Acoust. Soc. Am. **145**, 36 (2019).
[50] J. J. Faran, Sound scattering by solid cylinders and spheres, J. Acoust. Soc. Am. **23**, 405 (1951).
[51] R. Hickling, Analysis of echoes from a solid elastic sphere in water, J. Acoust. Soc. Am. **34**, 1582 (1962).
[52] D. T. Blackstock, *Fundamentals of Physical Acoustics* (John Wiley & Sons Inc., New York, 2000).
[53] P. Glynne-Jones, P. P. Mishra, R. J. Boltryk, and M. Hill, Efficient finite element modeling of radiation forces on elastic particles of arbitrary size and geometry, J. Acoust. Soc. Am. **133**, 1885 (2013).
[54] C. E. M. Démoré, P. M. Dahl, Z. Yang, P. Glynne-Jones, A. Melzer, S. Cochran, M. Macdonald, and G. C. Spalding, Acoustic Tractor Beam, Phys. Rev. Lett. **112**, 1 (2014).
[55] V. A. Khokhlova, P. V. Yuldashev, P. B. Rosnitskiy, A. D. Maxwell, W. Kreider, M. R. Bailey, and O. A. Sapozhnikov, Design of HIFU transducers to generate specific nonlinear ultrasound fields, Phys. Procedia **87**, 132 (2016).
[56] M. A. Ghanem, A. D. Maxwell, W. Kreider, B. W. Cunitz, V. A. Khokhlova, O. A. Sapozhnikov, and M. R. Bailey, Field characterization and compensation of vibrational nonuniformity for a 256-element focused ultrasound phased array, IEEE Trans. Ultrason. Ferroelectr. Freq. Control. **65**, 1618 (2018).
[57] K. Melde, A. G. Mark, T. Qiu, and P. Fischer, Holograms for acoustics, Nature **537**, 518 (2016).
[58] S. D. Mellin and G. P. Nordin, Limits of scalar diffraction theory and an iterative angular spectrum algorithm for finite aperture diffractive optical element design, Opt. Soc. Am. **8**, 1058 (2001).
[59] O. A. Sapozhnikov, S. A. Tsysar, V. A. Khokhlova, and W. Kreider, Acoustic holography as a metrological tool for characterizing medical ultrasound sources and fields, J. Acoust. Soc. Am. **138**, 1515 (2015).
[60] P. K. Kundu and I. M. Cohen, *Fluid Mechanics*, 3rd ed. (Elsevier Inc., San Diego, 2004).
[61] R. Marchiano and J.-L. Thomas, Synthesis and analysis of linear and nonlinear acoustical vortices, Phys. Rev. E **71**, 1 (2005).
[62] P. Z. Dashti, F. Alhassen, and H. P. Lee, Observation of Orbital Angular Momentum Transfer Between Acoustic and Optical Vortices in Optical Fiber, Phys. Rev. Lett. **96**, 1 (2006).
[63] J. Lekner, Acoustic beams with angular momentum Acoustic beams with angular momentum, J. Acoust. Soc. Am. **120**, 3475 (2006).
[64] L. Zhang and P. L. Marston, Acoustic radiation torque on small objects in viscous fluids and connection with viscous dissipation, J. Acoust. Soc. Am. **136**, 2917 (2014).
[65] K. D. Skeldon, C. Wilson, M. Edgar, and J. Padgett, An acoustic spanner and its associated rotational Doppler shift, New J. Phys. **10**, 1 (2008).
[66] Z. Hong, J. Zhang, and B. W. Drinkwater, Observation of Orbital Angular Momentum Transfer from Bessel-Shaped Acoustic Vortices to Diphasic Liquid-Microparticle Mixtures, Phys. Rev. Lett. **114**, 1 (2015).
[67] I. V. Basistiy, V. Y. Bazhenov, M. S. Soskin, and M. V. Vasnetsov, Optics of light beams with screw dislocations, Opt. Commun. **103**, 422 (1993).
[68] I. Freund, Critical point explosions in two-dimensional wave fields, Opt. Commun. **159**, 99 (1999).
[69] C. Shi, M. Dubois, Y. Wang, and X. Zhang, High-speed acoustic communication by multiplexing orbital angular momentum, Proc. Natl. Acad. Sci. **114**, 11 (2017).
[70] V. Bollen, D. J. Zartman, T. M. Marston, and P. L. Marston, Measured scattering of a first-order vortex beam by a sphere: cross-helicity and helicity-neutral near-forward scattering and helicity modulation, Proc. Meet. Acoust. **19**, 1 (2013).